Materials Advances

Accepted Manuscript

This article can be cited before page numbers have been issued, to do this please use: S. cosentino, M. Urso, G. Torrisi, S. Battiato, A. Terrasi and S. Mirabella, *Mater. Adv.*, 2020, DOI: 10.1039/D0MA00467G.

ROYAL SOCIETY OF CHEMISTRY

rsc.li/materials-advances

View Article Online
DOI: 10.1039/D0MA00467G

Abstract

High intrinsic activity of oxygen evolution reaction in low-cost NiO nanowalls electrocatalyst

S. Cosentino[1*], M. Urso[2*], G. Torrisi[2], S. Battiato[2], F. Priolo[2], A. Terrasi[2] and S. Mirabella[1,2]

[1] IMM-CNR and Università di Catania, via S. Sofia 64, 95123, Catania, Italy

[2]Dipartimento di Fisica e Astronomia "Ettore Majorana", Università di Catania, via S. Sofia 64, 95123, Catania, Italy

Earth-abundant materials for electrochemical water splitting typically show lower efficiency than noble and rare metal electrocatalysts. Nanostructuring and proper material design can largely improve the performances of low-cost electrocatalysts, opening the route towards a profitable mass production. Here, we report a quantitative investigation of oxygen evolution reaction (OER) on Ni-based nanowalls (NW) electrodes. NiO or $Ni(OH)_2$ NW film (200 or 400 nm thick) are produced by chemical bath deposition followed by calcination at 350°C. Morphology and chemical arrangement of NW were studied, before and after OER, by scanning electron microscopy, energy dispersive X-ray analysis and X-ray photoelectron spectroscopy. OER electrocatalytic activity was investigated by electrochemical measurements under alkaline conditions (1M KOH), demonstrating a stable overpotential of 345 mV at 10 mA/cm^2, a Tafel slope of 48 mv/dec and an O_2 turnover conversion frequency (TOF) up to 0.18 s^{-1}. A quantitative measurement of active electrocatalysts, through cross-correlations of experimental data, shows a nearly 100% material utilization in the 200 nm NiO NW. In thicker NiO or $Ni(OH)_2$ NW films this fraction decrease below 60%, probably due to electric potential drop along the nanostructure, as revealed by numerical simulation. These data and discussion support the employment of low-cost Ni-based nanostructures for high-efficiency and sustainable electrocatalysts.

**These two authors contributed to this work equally.*

View Article Online
DOI: 10.1039/D0MA00467G

Introduction

Electrochemical water splitting represents a pivotal technology to produce energy in a sustainable, clean and diffuse way [1-4]. The process of water splitting typically proceeds through two half reactions occurring at two electrodes: the cathodic hydrogen evolution reaction (HER) and the anodic oxygen evolution reaction (OER), which in case of alkaline media can be summarized as [1,2]:

$$4H_2O + 4e^- \rightarrow 2H_2 + 4OH^- \text{ and } 4OH^- \rightarrow O_2 + 2H_2O + 4e^-$$

The main intrinsic limitation of this technology is related to the poor efficiency of the OER process, associated with slow reaction kinetics and high values of overpotential required for the formation of O_2 through several intermediate reactions [1,5,6]. A low efficiency of OER is potentially detrimental also for HER process and final H_2 conversion, since the two half-reactions proceed together in a complete electrochemical water splitting device. Up to date, Ir- and Ru- oxides are the best reference electrocatalysts known for OER, while Pt coated electrodes are used to efficiently drive HER [1,4,7]. However, the cost and low abundance of these electrocatalysts poses questions on their large scale usage and thus large efforts have been directed towards the development of effective catalysis by using nanostructured and Earth abundant materials [4]. Among the plethora of materials and compounds recently proposed as low-cost OER electrocatalyst [7-10], transition metal oxides and oxy-hydroxide nanomaterials are unquestionably promising candidates in large scale electrochemical water splitting [11-13]. In particular, Ni-oxide nanomaterials are well-assessed Earth abundant materials for efficient OER, especially in combination with other metal dopants [4, 5, 11, 14-16]. NiO-based nanostructures have already shown very proficient catalytic actions in sensing, electrochromic smart windows, supercapacitors and energy applications [17-23]. Such material has high potential to work also as efficient backbone-platform electrocatalyst for both HER and OER. Doping or alloying with Fe, Co, Mn, showed to largely improve the performance of Ni electrocatalyst for OER, probably due to the optimization of the OH^- bonding within the active sites [11,14]. On the other side, alloying Ni with P, or Mo showed beneficial effect also for HER [24-27]. Ni based nanostructures are thus extremely appealing as a full water splitting cell can be realized with bi-functional heterogeneous electrocatalytic sites for HER and OER [16]. It has been recently shown that Ni-Co-Fe sulphides nanosheets onto Ni nanocones act as high performance electrocatalyst for total electrochemical water splitting at the potential of 1.54 V to give the current density of 10 mA/cm^2 [28]. Similarly, Fe^{2+}-doped layered double (Ni, Fe) hydroxides were used for overall water splitting showing an overpotential of 1.54 V to give a current density of 10 mA·cm^{-2} [29]. In photoelectrochemical water splitting the superior performances of Ni nanostructures in comparison to Ni dense material has been largely shown and attributed to a more effective charge transfer process [30, 31].

Actually, there is currently a great effort within the material science community in finding electrocatalysts with superior performance for water splitting, and the nanotechnology approach greatly supports the progress in this direction [4, 5, 16]. Nonetheless, while many papers report encouraging enhancements of the catalytic action when the Ni(oxide) nanostructures is mixed with other elements, a net discrimination of the doping effect over the nanostructure advantages and a fundamental understanding of both are sometimes missing. In addition, a high loading of material electrocatalysts, as typically occurs for Earth abundant elctrocatalysts, could be as expensive as for noble-metal electrocatalysts due to their lower intrinsic activity [4]. This points out that for a real large scale usage of water splitting methods, a clear determination of the mass activity is needed. Moreover, a fair comparison among literature data and reproducible results are still quite a challenge. It was magisterially shown that just a few nanomolar of Ni and Fe impurity in the electrolyte solution, coming from contaminated chemicals or glassware, is able to give rise to OER current up to 1 mA at overpotential of 400 mV [32, 33]. Therefore, controlled and reproducible experiments with quantitative metrics, and hopefully a solid understanding of the underlying mechanism, are urgently needed when a new performant electrocatalyst is claimed [1]. Besides the ability to drive an efficient synthesis of nanostructures and to obtain the best usage of material resources, it would be as much as desirable to reliably measure the quantitative utilization of catalytic material, which could guide in developing specific shape, size and alloying of elements and compounds for efficient OER.

Here we report a detailed and quantitative investigation of the OER in low-cost synthesized Ni-oxides based nanowalls (NW) without any intentional doping. $Ni(OH)_2$ and NiO NW are synthesized through careful chemical bath deposition and show a highly textured surface leading to an effective ion exchange with the electrolyte. Electrochemical measurements show improved stability and high OER conversion efficiency in thin NiO NW, while significant unused material is estimated for thick NW films. A numerical modelling of the electrical potential distribution along the NW explains the more effective electrochemical activation of shorter NW, which are further corroborated by quantitative XPS analysis. These data and relative discussion give a new light to the basic mechanisms of OER process in Ni-based nanostructures.

Experimental

Particular care was taken to avoid any potential Fe contamination sources during all the experimental processes. $Ni(OH)_2$ NW were grown on cleaned substrates by chemical bath deposition (CBD) using new and Fe-free Teflon beakers. The substrates consist of thin films of Au (50 nm) on Ti (25 nm) grown on quartz substrates by sputtering deposition. Quartz substrates were chosen on purpose to avoid Fe contamination and were carefully cleaned with acetone, isopropanol and DI water and dried in N_2 before deposition. The chemical solution for CBD was prepared by mixing 0.42 M $NiSO_4 \cdot 6H_2O$ (Alfa Aesar, 98%), 0.07 M $K_2S_2O_8$ (Alfa Aesar, 97%) and 3.5 wt% ammonia (Merck, 30–33 wt% NH_3 in H_2O) in DI water [22]. The solution was heated up

to 50 °C and kept at this temperature through a bain-marie configuration. Substrates were immersed in the CBD solution for a period of time ranging from 3 to 20 min, in order to achieve the growth of $Ni(OH)_2$ NW films with different thickness. Then, the samples were rinsed with deionized water to wash deposited film from unwanted microparticulate and dried in N_2. Some samples were further annealed at 350 °C for 60 min in Ar in order to get calcination of films and obtain NiO NW, as confirmed by XRD [17]. Film mass after each synthesis step was measured with a Kern ABT-100 5NM (sensitivity of 0.01 mg) quartz micro-balance (QCM).

The surface morphology and sample thickness were characterized by using a scanning electron microscope (Gemini field emission SEM Carl Zeiss SUPRA 25) combined with energy dispersive X-ray spectroscopy (EDX).

Electrochemical analyses were performed using a Versastat-4 potentiostat in a three-electrode setup with a Pt wire as a cathode, a saturated calomel electrode (SCE) as a reference electrode, and Ni-based NW film as working electrode. All measurements were performed at room temperature and atmospheric pressure, in a one-compartment electrochemical Teflon cell filled with 100 ml of 1 M KOH (measured pH = 13.5) as supporting electrolyte.

The potential distribution along the NW was numerically simulated by using the COMSOL Multiphysics software [34]. To simulate the NW electrode, a 20 nm thick NiO nanosheet was designed, while a bulk Au substrate was conceived as current collector for the electrode. The following room temperature conductivities were used: 10^{-4} S cm^{-1} for NiO, 0.2 S cm^{-1} for 1 M KOH and electrical permittivity of 11.9 for NiO [35,36] . A steady-state model was employed to evaluate the electric field distribution across the electrode at a constant applied voltage of 1.6 V.

X-ray Photoelectron Spectroscopy (XPS) analysis was employed to investigate the oxidation state evolution of NW before and after OER. XPS spectra were obtained using Al kα photon source (1486.7 eV) and a hemispherical electron analyzer VG Microtech CLAM4 equipped with a multi-channeltron detector (MCD). The kinetic energy of the photoelectrons emitted from the sample surface were collected with a 20 eV pass energy, resulting in a line spectra resolution of about 1.2 eV. The Au $4f_{7/2}$ was used as calibration peak at 84.0 eV. The deconvolution and fitting of peaks were carried out with fityk software [37].

Results and Discussions

$Ni(OH)_2$ and NiO NW were synthesized through a two-steps process, as schematized in the top panel of figure 1. The first step involves a CBD at 50°C to ensure the growth of $Ni(OH)_2$ NW on top of the Au (50 nm)/Ti (25 nm)/quartz substrate. The second step consists in a post-growth thermal annealing in Ar at 350°C for 1h, which induces the de-hydration of $Ni(OH)_2$ into NiO. Figure 1Sa reports the SEM image of the pristine $Ni(OH)_2$

NW film, which consists of a densely interconnected array of thin (~20-30 nm) sheets mostly perpendicular to the substrate [18]. The $Ni(OH)_2$ NW film has a very high surface area of 30-40 m^2/g, as measured previously by BET gas adsorption measurements [17]. By increasing synthesis time, the NW film thickness increases from 200 nm for 3 min, to 400 nm for 20 min growth time (table 1S and figure 2S). Notably, the morphology of annealed NiO NW films does not appreciably change compared to the pristine $Ni(OH)_2$ NW (figure 1S), neither after OER as shown in figure 1(a). In addition, EDX analysis, figure 1(b)-(c), confirmed that the NW composition is solely constituted by Ni and O. EDX peaks of Au and Ti are ascribed to the underneath electrode substrate. Contamination of K from the electrolyte solution appears for samples after electrochemical OER, while no traces of Fe were detected within the resolution of the EDX (<0.1%) as shown in the inset of figure 1(d), both before and after OER (figure S3) analysis.

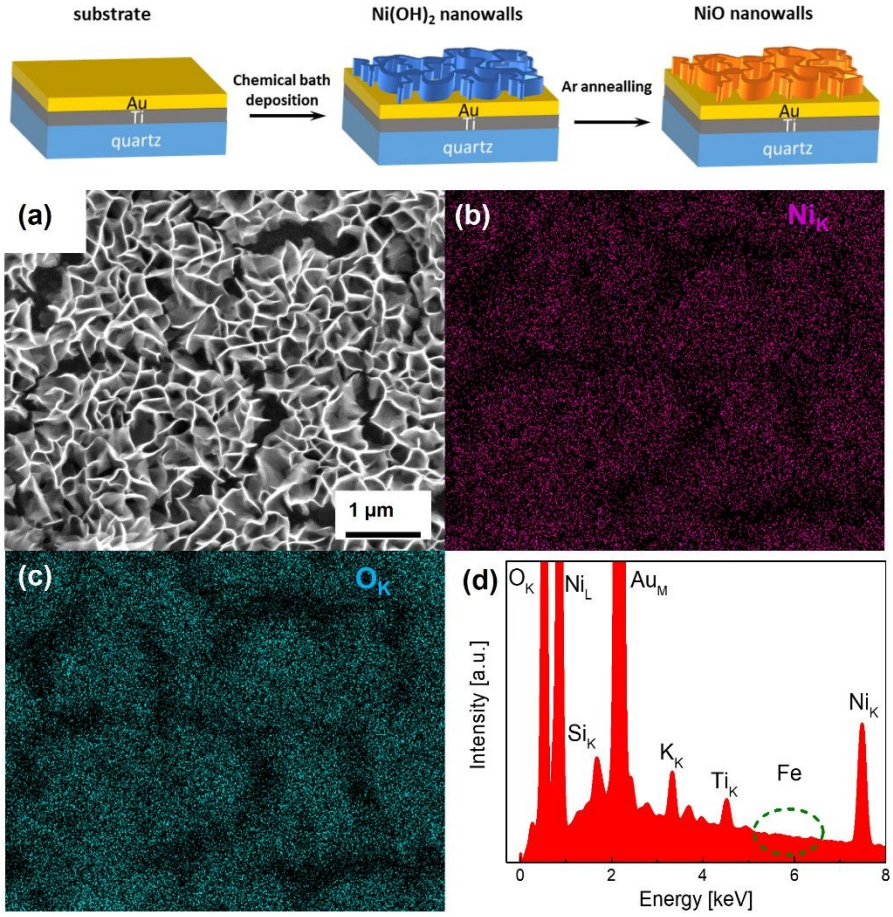

Figure 1: SEM image of NiO NW (a), and corresponding EDX-SEM colour map for Ni (b) and O (c) atomic signals, together with EDX survey (d).

In order to measure the performances of $Ni(OH)_2$ and NiO NW electrocatalysts toward OER, we performed a series of electrochemical measurements. In particular, each NW electrode was electrochemically characterized using the following series of tests: 1) electrochemical impedance spectroscopy (EIS); 2)

cyclic voltammetry (CV); 3) EIS, 4) Tafel analysis (chronopotentiometry, CP); 5) EIS; 6) chronoamperometry (10 min); 7) CV and (8) CP stability test for 5h. The measured potential was converted to the overpotential, η', against the reversible hydrogen electrode (RHE) according to the relationship [38, 39]:

$$\eta' = E_{RHE} - 1.23 = E_{SCE} + E^0_{SCE} + ln\,10\frac{RT}{F} \cdot pH$$

where E_{RHE} and E_{SCE} are the potential of the working electrode with respect to the RHE and SCE, respectively. E^0 is the standard reduction potential of the reference electrode with respect to the RHE, while R, T, and F are the gas constant, temperature, and Faraday constant. Moreover, the overpotential was also corrected for the uncompensated series resistance as follows:

$$\eta = \eta' - iR_u$$

where i is the current collected at the electrode, while R_u [Ohms] is the intercept on real axis of Nyquist plots (real vs imaginary part of the impedance, Z) obtained from EIS measurements performed in a frequency range between 1 Hz and 100 kHz at 0V vs. open circuit potential (see figure S4 in supplementary info)[38].

Figure 2 reports the CV curves recorded for $Ni(OH)_2$ NW and for two different thicknesses of NiO NW electrocatalyst. Two pronounced oxidation and reduction peaks appear for all samples, which are attributed to the redox couple Ni^{2+}/Ni^{3+}. At higher values of overpotential, a strong increase of current appears, due to OER occurring at the electrocatalyst surface. Upon this regard, the pristine $Ni(OH)_2$ NW electrode shows only a moderate activity which is also accompanied by some electorcatalyst deterioration (figure S5). On the other side, NiO NW electrocatalysts show higher current at lower overpotential and increased stability. The latter is probably due to an increased stiffness of NW film after calcination.

It is important to remind that both NiO and $Ni(OH)_2$ follow a similar redox reaction, which can be simplified with a single-electron reaction as [40, 41]:

$$Ni(OH)_2 + OH^- \leftrightarrows NiOOH + H_2O + e^- \quad (1)$$
$$NiO + OH^- \leftrightarrows NiOOH + e^-$$

Moreover, in Fe-free Ni oxides, NiOOH and especially its γ phase is often described as the potential active electrocatalyst for OER [42, 43]. In particular, γ-NiOOH has a layered structure consisting of NiOOH planes and intercalated water molecules or ions, with a larger interplanar distance than β-NiOOH [44, 45]. This results in a higher Ni oxidation state in γ-NiOOH (3.5-3.67) than β-NiOOH (3), and thus in superior catalytic activity [42]. Such peculiar structural characteristic is morphologically accompanied with the high surfaces exposed by our NW film, which is optimal to involve a larger amount of atoms in the OER process than bulky electrocatalyst

films. Moreover, several studies recently reported that minimal impurities of Fe were sufficient to improve the catalytic activity of $Ni(OH)_2$ [32,33], giving rise to OER current of around 1 mA at 400 mV of overpotential. Although SEM-EDX and XPS analysis did not show any signal due to significant iron contamination both before and after electrochemical measurements, still Fe traces below the detection limit (<0.1%) cannot be completely excluded. However, we expect that the effect of such Fe contamination, if any, would be small and similar for all the investigated samples, keeping still valid both the activity metrics and later discussion.

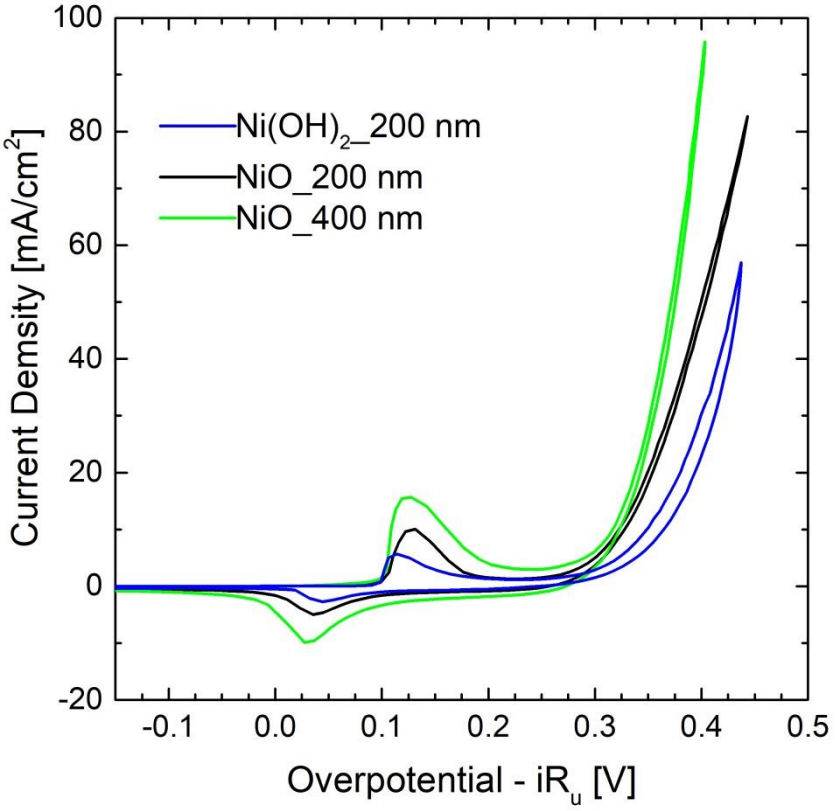

Figure 2: CV curves of $Ni(OH)_2$ and NiO NW films deposited on Au/Ti/quartz substrates. All curves refer to the 10th cycle and overpotential was corrected for the uncompensated resistance estimated from EIS measurements.

The stability of NW electrodes was evaluated by running CP measurements with the electrodes kept at a current density of 10 mA/cm² for five hours, while overpotential changes were recorded. Figure S6 shows a different behavior between NiO and $Ni(OH)_2$ NW. $Ni(OH)_2$ NW shows poor stability, with an overpotential stably increasing over time and exceeding the value of 420 mV after 5h of OER activity. On the contrary, NiO NW films show an improved electrochemical stability, with both the 200-nm and the 400-nm thick NW evidencing a nearly constant overpotential of around 345 mV and 350 mV, respectively. Similarly to what observed during CV tests, such improved stability is probably related to a better stiffness of the NiO NW film to the bulk support electrode.

The different behavior observed in CV and CP measurements between NiO and $Ni(OH)_2$ NW films is related to a different activity of the electrocatalyst towards OER. To compare activity of various electrocatalysts towards water splitting, the overpotential at a current density of 10 mA/cm^2 is often used [1, 39]. In this regards, as already clearly visible in figure 2 and 3, one can generally conclude that NiO NW performs better than $Ni(OH)_2$ NW and the reaction becomes more effective when a thicker ~400 nm NW electrocatalyst is used, since both overpotential and stability are optimized. However, relying only on values of overpotential can be misleading since that is an intensive quantity and it is not quantitatively linked to the amount of active material being involved in OER. For this reason, steady-state Tafel equation was also used from chronopotentiometry measurements to calculate activity metrics. Generally, a smaller Tafel slope implies faster electrochemical kinetics [46, 47]. The Tafel slopes extrapolated from linear fit of data points below 10 mA/cm^2 are shown in figure 3(a). $Ni(OH)_2$ NW exhibits a slope of around 104 mV/dec, while both NiO NW electrodes exhibit a similar slope of around 50 mV/dec. The lower slope of NiO NW compared to $Ni(OH)_2$ NW might be related to a different OER process pathway. In fact, a Tafel slope around 120 mV/dec is typically observed when reaction proceeds as $M+OH^- \rightarrow MOH + e^-$, where M denotes an active site on the surface [47]. However, when the surface has already some adsorbed OH species the reaction is found to proceed at a lower Tafel slope, typically around 30-40 mV/dec [47]. In this regard, it was recently shown that the increased electrochemical kinetics of NiO_x structures compared to $Ni(OH)_2$ is related to an increased amount of oxygen vacancies and point defects, favouring the adsorption of hydroxide groups and driving OER at a lower energy rate step [15, 40, 42]. This would lead to a more favourable formation of NiOOH complexes at the electrocatalyst surface and to a more effective OER process. Moreover, also the better stiffness of NiO NW might help in improving the electrochemical stability of the entire film at high current density.

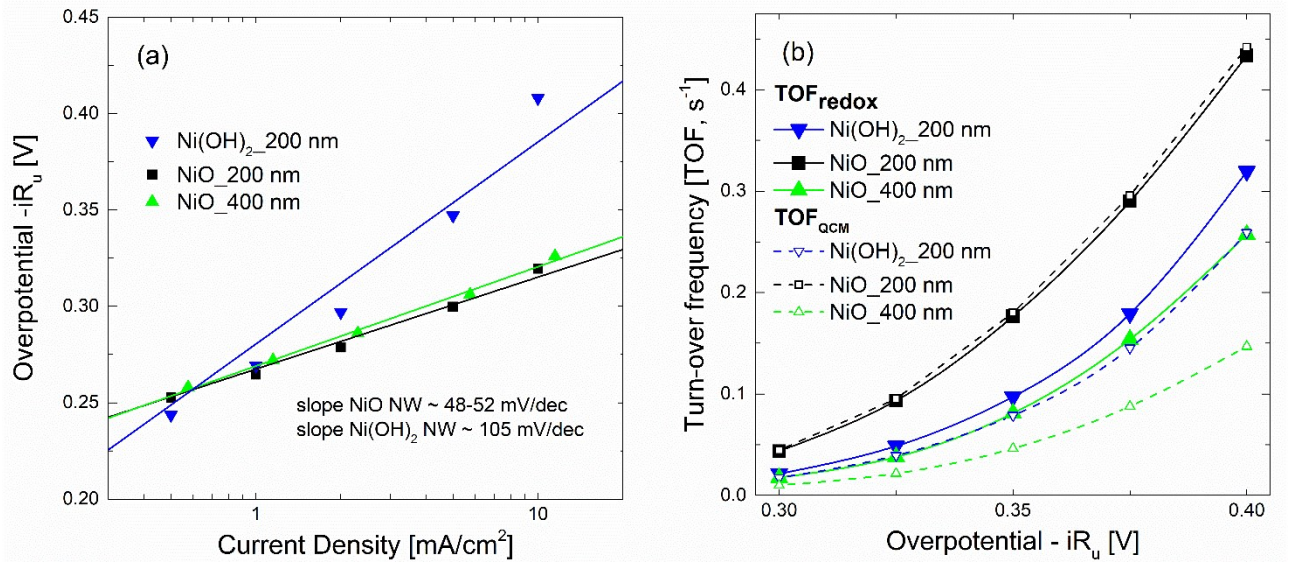

Figure 3: Steady-state Tafel plots (a) and turn-over frequency (TOF) curves (b) of $Ni(OH)_2$ and NiO NWs films. The values of overpotential of Tafel analysis were acquired from CP measurements in steps from 0.05 mA/cm^2 to 10 mA/cm^2, each held for 3 min. TOF values were calculated considering the number of active sites extracted from electrochemical measurements (TOF_{redox}), or measured by QCM (TOF_{QCM}).

View Article Online
DOI: 10.1039/D0MA00467G

To shed more light on the different activity between $Ni(OH)_2$ and NiO NW films, we also extracted more quantitative information on the amount of electrocatalyst participating to OER by the analysis of the oxidation peak in the CV curves. As shown in figure 2, a clear difference among investigated samples appears in the intensity of the redox peaks, which is intimately related to a different electro-catalytic activity. In fact, the area underneath the peak is proportional to the amount of active electrocatalytic sites available for the OER process [39, 48]. The current *i* recorded during CV is a measure of the charge Q passed over a period of time: $= {}^{dQ}/_{dt}$. Given that current sweep is acquired at a given scan rate, $= {}^{E}/_{t}$, the integration of the current peak returns the amount of charge passed through the electrode during the redox reaction. This relationship is valid with the assumption that the redox reaction is a one-electron transfer as written in reaction (1). In our case, $Ni(OH)_2$ NW electrode exhibits the smallest area of the peak, corresponding to an amount of 1.7×10^{17} active sites/cm^2. Instead, NiO NW have an amount of active sites increasing from 2.8×10^{17} sites/cm^2 (200 nm), to 5.6×10^{17} sites/cm^2 (400 nm), as reported in table 1.

Table 1: Activity Metrics of $Ni(OH)_2$ and NiO NW electrocatalysts.

	$Ni(OH)_2$_200 nm	**NiO_200 nm**	**NiO_400 nm**
Overpotential at 10 mA/cm^2 [mV]	420	345	350
Tafel slope [mV/dec]	104	48	52
Number of active sites [$\times10^{17}$ cm^{-2}]	1.7	2.8	5.6
Total active electrocatalyst [µmol·cm^{-2}]	0.28	0.46	0.91
Fraction of active electrocatalyst [±10%]	80%	~100%	57%
Current Density at η=350 mV [A/cm^2]	7.05×10^{-3}	20.1×10^{-3}	28.5×10^{-3}
TOF at η=350 mV [s^{-1}]	9.7×10^{-2}	1.8×10^{-1}	8.1×10^{-2}

The number of active electroatalytic sites determined from electrochemical measurements are in good agreement with the total density of electrocatalyst, as obtained from QCM measurements and reported in table 1s. In particular, for both the 200 nm samples, the number of active electrocatalyst closely matches that obtained by QCM. This means that nearly all atoms are participating to OER process, confirming that nanostructures are effective for material utilization. In fact, the porous-like 3D morphology of our NW thin films is of great help to optimize the amount of electrocatalysts ionically connected to OH^- groups and electronically connected to the current collector. Nonetheless, it is worth noting that the thicker NiO NW has

a lower fraction of active electrocatalyst, suggesting a limited effectiveness of the OER process. To better investigate the metrics relevant to intrinsic activity of electrocatalysts in OER, the turn-over frequency (TOF) must be considered [4]. The TOF is defined as the rate of production of oxygen molecules per available (and active) site:

$$TOF = {}^{I}/_{4nF}$$

where *I* is the measured current at a certain overpotential, *F* is the Faraday constant (96485 *C* mol^{-1}) and *n* is the number of moles of available (active) sites determined from QCM (TOF_{QCM}) or by the redox peak integration (TOF_{redox}). It should be noted that, unfortunately, literature data are usually biased towards record activity claiming and often discarding the amount of available site and the activity of each catalytic site [4]. The TOF_{QCM} and TOF_{redox} are extremely useful metrics to determine the activity of each site, even if on average scale, considering the full electrocatalyst loading or the redox active one, respectively. A higher TOF is desirable since each available site produces more O_2 molecules per unit time, as well as a convergence between TOF_{QCM} and TOF_{redox}, is wished for a better material utilization. Figure 3(b) reports the trends of TOF_{QCM} and TOF_{redox} values in the 300 ÷ 400 mV overpotential range. Clearly, the TOF increases with applied overpotential for kinetics reasons, still the number of active sites really matters for defining the effectiveness of OER process. The 200 nm-thin NiO NW film always shows the higher values of TOF and a nice convergence of TOF_{QCM} and TOF_{redox}, meaning that on average all active sites are available to activate an effective OER. As reported in table 2, a TOF of 0.18 s^{-1} is obtained at 350 mV of overpotential. Although the $Ni(OH)_2$ NW film has a fraction of active electrocatalyst comparable to that of 200 nm-thin NiO NW film, its TOF values are systematically lower as demonstrated by its minor OER current. Increasing the thickness of NiO NW film leads to the expected increase of current density, still the material utilization decreases as shown by the considerably reduced TOF. Such behavior reveals that increasing thickness of NW film does not always produce a corresponding rise of the intrinsic OER performance, because of lower percentage of active electrocatalyst. In thicker NW, electrochemical properties are in somehow weakened, leading to a less effective material utilization. The highest mass activity has been found for the 200 nm thin NiO NW film with a remarkable value of 0.33 A/mg at the current of 10 mA/cm^2 with overpotential of 345 mV. The measured activity metrics of all our samples are considerably higher, or among the highest performances reported in literature for NiO based electrocatalysts, as shown in table 2. Indeed, our NiO NW electrocatalyst shows the best combination because of its low values of overpotential and Tafel slope and the high TOF.

View Article Online
DOI: 10.1039/D0MA00467G

Table2: Activity metrics of NiO based electrocatalyst for OER.

Electrocatalyst material	Electrolyte	Overpotential (mV) at 10mA/cm²	Tafel Slope (mV dec⁻¹)	TOF (s^{-1}) at η=350 mV	Electrode	Reference
NiO hollow nanofibers	1 M KOH	322	78	0.07	Ni foam	[49]
α–$Ni(OH)_2$ nanospheres	0.1 M KOH	331	42	0.036	Glassy carbon	[50]
NiTi Oxide nanosheets	1 M KOH	320	52	0.005	Glassy carbon	[51]
NiO nanowalls	1 M KOH	310	54	NA	Nickel foam	[52]
NiO thin films	0.5 M KOH	360	30	0.07	ITO	[53]
$Ni(OH)_2$ nanoplates	0.1 M KOH	474	87	0.015 (at 490 mV)	ITO	[54]
Ni/NiO nanoparticles	1 M KOH	320	61	0.11	Glassy carbon	[55]
NiO_x films	1 M KOH	380	42	NA	Glassy carbon	[56]
NiO nanosheets	0.1 M KOH	422	116	NA	Carbon Cloth	[57]
NiO nanosheets	1 M KOH	320	52	NA	Graphene	[58]
NiO nanowalls	**1 M KOH**	**345**	**48**	**0.18**	**Quartz/Ti/Au**	**This work**

In order to study the origin of higher activity for smaller NiO NW, the electric potential field distribution along the NW electrode during electrochemical activity was simulated by using the COMSOL Multiphysics software. A simulation on such a macroscopic quantity can give valuable understanding on the basic processes occurring at the nanoscale. The results of the applied potential distribution across the NW are presented in figure 4 in a false colour scale from 1.3 to 1.6 V. The 200 nm-thin NW displays a nearly uniform potential field along its structure, with a minimal potential drop, lower than 0.1 V, near the top region of the NW. By doubling the NW length, a considerably larger potential drop is found, with NW tip at a potential 0.3 V below the Au contact. This effect is detrimental for OER since only a portion of the material is at a potential high enough to achieve the electrochemical reaction. This effect helps explaining the reduced activity metrics evaluated for thicker NW film electrodes. Only the region close to the NW-substrate interface experiences a potential high enough to efficiently drive the OER process. On the top region of the longer NW, the potential field is reduced to a level close the thermodynamic limit for OER of 1.23 eV, for which the reactions can only poorly occur.

View Article Online
DOI: 10.1039/D0MA00467G

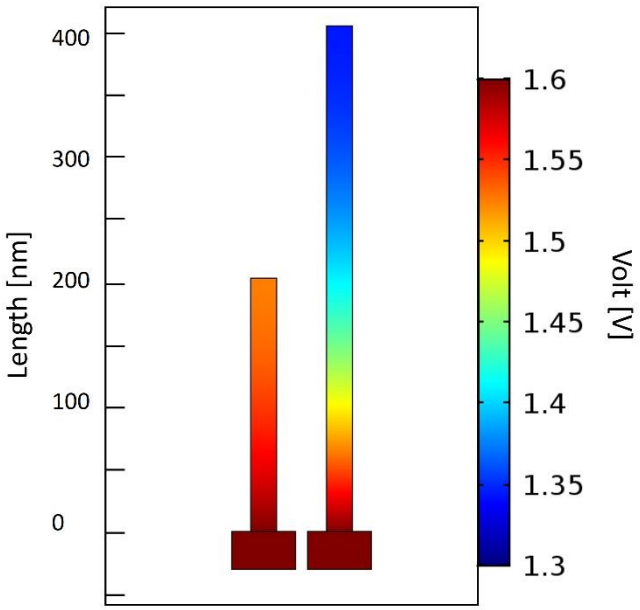

Figure 4: Electric potential distribution in the NiO NW electrodes with different NW size in 1 M KOH solution for 1.6 V of applied bias, as simulated by COMSOL Multiphysics software. A 20 nm thick and 200 (or) 400 nm tall NiO nanosheet was used to simulate the NiO NW electrodes.

Finally, to compare the OER activity of NiO NW with the chemical evolution at the electrode surface, we performed XPS analysis on the 400 nm-thick NiO NW film electrode before and after OER. In particular, the NiO NW electrode run a CP test at 10 mA/cm^2 for 1 h just before to be introduced into the XPS analysis chamber. This was done with the intention to verify whether the lower TOF estimated the thicker NW film is related to incomplete chemical transformation of the electrocatalyst and to the presence of inert material. Figures 5 shows the Ni $2p_{3/2}$ and O 1s spectra of NiO NW before and after OER. The quantification and interpretation of XPS peak shape of Ni-based oxides is not trivial, due to the presence of extended multiplets, shake-up and plasmon loss structures, which can be confused with the overlapping of different chemical states of Ni [59-61]. For the XPS data fitting, the extensive study done by Biesinger et al. was used as guideline[60]. They concluded that the full Ni 2p photoemission envelope, for pure Ni^{2+} species (e.g., NiO or $Ni(OH)_2$) and pure Ni^{3+} species (e.g., γ-NiOOH) can be fit with a unique set of seven components [60, 61]. Binding energies, peak distances and FWHM were kept fixed in our fitting, according to values given by Biesinger et al. [60], while only peak intensities were used as free parameters. Fit values are summarized in table 2S of the supplementary info.

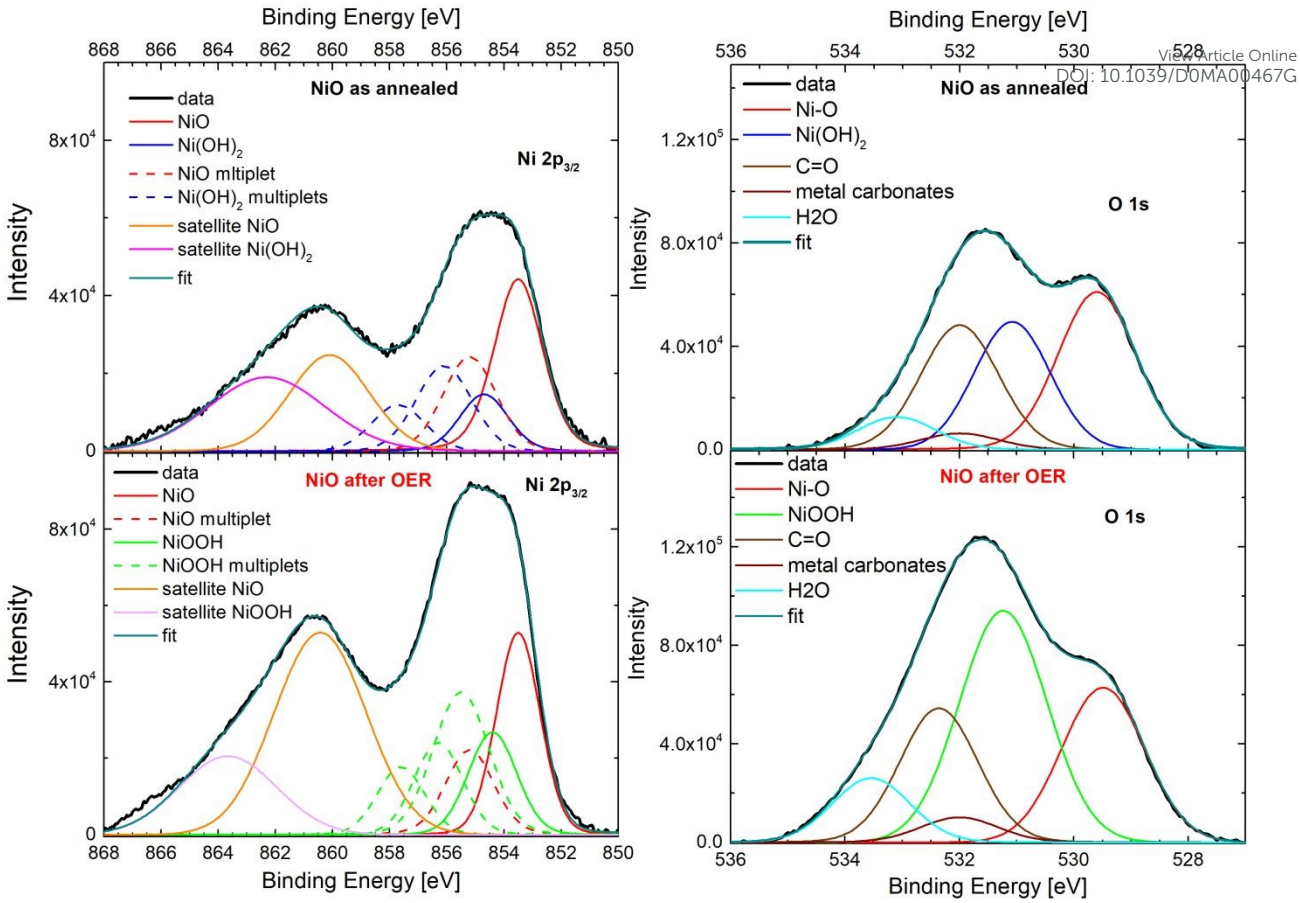

Figure 5: XPS spectra of 400-nm thick NiO NW electrocatalyst. Ni $2p_{3/2}$ (a) and O 1s (b) for NiO NW before OER. Ni $2p_{3/2}$ (c) and O 1s (d) for NiO NW after OER.

Figure 5(a) shows the Ni $2p_{3/2}$ spectra of NiO NW before OER (as annealed). The broad peak in the range between 852 and 858 eV is due to the overlap of a NiO component (main peak at 853.6 eV and multiplet at 855.2 eV) with $Ni(OH)_2$ multiplet peaks, while the broad shoulder between 858 and 868 eV is due to the satellite peaks of NiO and $Ni(OH)_2$. The presence of peaks related to $Ni(OH)_2$ states in NiO films is not unexpected, since hydroxide groups can readily adsorb on the surface because of ambient moisture [58]. Interestingly, the same information comes also from the O 1s peak shown in figure 5(b), where the peak at 529.6 eV is related to Ni-O bond and is accompanied by a peak at 531.1 due to $Ni(OH)_2$, together with adventitious contamination peak at 532 eV and water adsorbates at around 533.3 eV. From both Ni 2p and O 1s spectra, the ratio of the intensities of the components related to $Ni(OH)_2$ and NiO peaks (see table 2S in supplementary info) indicates that about 40% of the Ni atoms in NiO NW film before OER is actually in the chemical state of $Ni(OH)_2$. Therefore, it is reasonable to assume that freshly annealed NiO NW have thin shell of $Ni(OH)_2$ of few nm surrounding the NiO core. The presence of such bimodal chemical composition of Ni atoms is kept also in the Ni 2p and O 1s XPS spectra of the NW electrode after OER, as shown in figure 5(c) and (d). The presence of NiO is confirmed by the peak at 853.5 eV for Ni $2p_{3/2}$ and at 529.5 eV for O 1s spectra. However, as especially evident for the O 1s spectrum, a larger signal comes from Ni^{3+} species due to the presence of NiOOH. From a quantitative analysis of the intensities of the peaks related to NiO and NiOOH, it

is possible to estimate that NiOOH constitutes only about 60% of the overall composition of the NW electrode after OER. Such a value is a further confirmation that a not negligible amount of atoms, around 40% of the total, does not follow the redox reaction and is not active towards OER in the thick NW film. Such an amount of inert atoms is perfectly in agreement with the estimations of inactive electrocatalyst in the electrochemical activity metrics and in conceptual agreement with the large potential drop calculated for the 400 nm-thick NW film.

Thus, for the design of novel Ni-based electrocatalyst, one should focus on optimizing the thickness of the electrocatalyst and increasing the amount of available electrocatalytic sites by increasing the total surface area, instead of indefinitely increase the thickness and the mass loading only.

Conclusions

We performed a quantitative investigation of OER process in highly textured $Ni(OH)_2$ and NiO NW films, synthesized by low-cost methods. Electrochemical measurements revealed that, in comparison to $Ni(OH)_2$, NiO NW film shows significant improvement of OER performance, with an overpotential of 345 mV and a Tafel slope as low as 48 mV/dec. The worthy performances of NiO NW are also supported by its high activity metrics, in terms of mass activity up to 0.33 A/mg and TOF value of 0.18 s^{-1} at 350 mV overpotential. By comparing NiO NW at different length, electrochemical measurements showed that a lower percentage of active sites is found, bringing down the overall OER performance. While nearly all available sites are active in a 200-nm long NW, in a longer 400-nm NW less than 60 % of electrocatalyst is involved in OER. A numerical simulation of electrical potential distribution and a detailed XPS analysis confirm that a large part of NiO in longer NW films remain in inert chemical state, probably because of a lower electric potential experienced. Such results contribute to build a solid understanding of OER mechanism in Ni-based nanostructures, and can help in defining a roadmap for material optimization in nanostructured electrocatalysts.

Conflict of Interest

All authors contributed to the final version of this paper. The authors declare that there is no conflict of interest regarding the publication of this article.

Acknowledgements

Sergio Battiato aknowledges the project AIM1804097 - Programma Operativo Nazionale FSE- FESR “Ricerca e Innovazione 2014-2020”.

References

1 I. Roger, M. A. Shipman and M. D. Symes, *Nature Reviews Chemistry*, 2017, *1(1)*, 1–13.

2 J. Ronge´, T. Bosserez, D. Martel, C. Nervi, L. Boarino, F. Taulelle, G. Decher, S. Bordiga and J. A. Martens, *Chemical Sociecty Reviews*, 2014, *43*, 7963–7981.

3 A. Landman, H. Dotan, G. E. Shter, M. Wullenkord, A. Houaijia, A. Maljusch, G. S. Grader and A. Rothschild, *Nature Materials*, 2017, *16(6)*, 646–651.

4 J. Kibsgaard and I. Chorkendorff, *Nature Energy*, 2019, *4(6)*, 430–433.

5 J.-W. Wang, W.-J. Liu, D.-C. Zhong and T.-B. Lu, *Coordination Chemistry Reviews*, 2019, *378*, 237–261.

6 T. Hisatomi, K. Takanabe and K. Domen, *Catalysis Letters*, 2015, *145(1)*, 95–108.

7 S. Chen, S. S. Thind and A. Chen, *Electrochemistry Communications*, 2016, *63*, 10–17.

8 X. Li, X. Hao, A. Abudula and G. Guan, *Journal of Materials Chemistry A*, 2016, *4(31)*, 11973–12000.

9 A. Shinde, D. Guevarra, J. A. Haber, J. Jin and J. M. Gregoire, *Journal of Materials Research*, 2015, *30(3)*, 442–450.

10 X. Zou and Y. Zhang, *Chemical Society Reviews*, 2015, *44(15)*, 5148–5180.

11 M. S. Burke, L. J. Enman, A. S. Batchellor, S. Zou, and S. W. Boettcher, *Chemistry of Materials*, 2015, *27(22)*, 7549–7558.

12 J. B. Gerken, S. E. Shaner, R. C. Massé, N. J. Porubsky, and S. S. Stahl, *Energy & Environmental Science*, 2014, *7(7)*, 2376–2382.

13 B. Zhang, X. Zheng, O. Voznyy, R. Comin, M. Bajdich, M. García-Melchor, L. Han, J. Xu, M. Liu, L. Zheng, F. P. G. de Arquer, C. T. Dinh, F. Fan, M. Yuan, E. Yassitepe, N. Chen, T. Regier, P. Liu, Y. Li, P. De Luna, A. Janmohamed, H. L. Xin, H. Yang, A. Vojvodic and E. H. Sargent, *Science*, 2016, *352(6238)*, 333–337.

14 D. Friebel, M. W. Louie, M. Bajdich, K. E. Sanwald, Y. Cai, A. M. Wise, M.-J. Cheng, D. Sokaras, T.-C. Weng, R. Alonso-Mori, R. C. Davis, J. R. Bargar, J. K. Nørskov, A. Nilsson, and A. T. Bell, *Journal of the American Chemical Sociecty*, 2015, *137(3)*, 1305–1313.

15 Q. Hu, X. Huang, Z. Wang, G. Li, Z. Han, H. Yang, X. Ren, Q. Zhang, J. Liu and C. He, *Journal of Materials Chemistry A*, 2020, *8(4)*, 2140–2146.

View Article Online
DOI: 10.1039/D0MA00467G

16 Y. Li, X. Bao, D. Chen, Z. Wang, N. Dewangan, M. Li, Z. Xu, J. Wang, S. Kawi and Q. Zhong, *ChemCatChem* 2019, *11(24)*, 5913–5928.

17 K. O. Iwu, A. Lombardo, R. Sanz, S. Scirè and S. Mirabella, *Sensors and Actuators B: Chemical*, 2016, *224*, 764–771.

18 M. Urso , G. Pellegrino, V. Strano , E. Bruno, F. Priolo and S. Mirabella, *Nanotechnology*, 2018, *29(16)*, 165601.

19 M. Urso, S. G. Leonardi, G. Neri, S. Petralia, S. Conoci, F. Priolo and S. Mirabella, *Sensors and Actuators B: Chemical*, 2020, *305*, 127481.

20 T. P. Mokoena, H. C. Swart and D. E. Motaung, *Journal of Alloys and Compounds*, 2019, *805*, 267–294.

21 X.H. Xia, J.P. Tua, J. Zhang, X.L. Wang, W.K. Zhang and H. Huang, *Solar Energy Materials & Solar Cells*, 2008, *92(6)*, 628–633.

22 M. Urso, G. Torrisi, S. Boninelli, C. Bongiorno, F. Priolo and S. Mirabella, *Scientific Reports*, 2019, *9*, 7736.

23 H. Lai, Q. Wu, J, Zhao, L. Shang, H. Li, R. Che, Z. Lyu, J. Xiong, L. Yang, X. Wanga and Z. Hu, *Energy & Environmental Science*, 2016, *9(6)*, 2053–2060.

24 J. Zheng, W. Zhou, T. Liu, S. Liu, C. Wang and L. Guo, *Nanoscale*, 2017, *9(13)*, 4409–4418.

25 M. Schalenbach, F. D. Speck, M. Ledendecker, O. Kasian, D. Goehl, A. M. Mingers, B. Breitbach, H. Springer, S. Cherevko and K. J. J. Mayrhofer, *Electrochimica Acta*, 2018, *259*, 1154–1161.

26 T. Wang, R. Jin, X. Wu, J. Zheng, X. Li and K. Ostrikov, *Journal of Materials Chemistry A*, 2018, *6(19)*, 9228–9235.

27 P. Jiang, Q. Liu and X. Sun, *Nanoscale*, 2014, *6(22)*, 13440–13445.

28 G. B. Darband, M. Aliofkhazraei, S. Hyun, A. S. Rouhaghdam and S. Shanmugam, *Nanoscale*, 2019, *11(35)*, 16621–16634.

29 X. Meng, J. Han, L. Lu, G. Qiu, Z. L. Wang and C. Sun, *Small*, 2019, *15(41)*, 1902551.

30 M. K. Bates, Q. Jia, H. Doan, W. Liang and S. Mukerjee, *ACS Catalysis*, 2016, *6(1)*, 155–161.

31 G. Huang, R. Fan, X. Zhou, Z. Xu, W. Zhou, W. Dong and M. Shen, *Chemical Communications*, 2019, *55(3)*, 377–380.

32 I. Roger and M. D. Symes, *Journal of the American Chemical Society*, 2015, *137(43)*, 13980–13988.

33 L. Trotochaud, S. L. Young, J. K. Ranney, and S. W. Boettcher *Journal of the American Chemical Society*, 2014, *136(18)*, 6744–6753

View Article Online
DOI: 10.1039/D0MA00467G

34 COMSOL Multiphysics® v. 5.3. www.comsol.com. COMSOL AB, Stockholm, Sweden

35 R. J. Gilliam, J. W. Graydon, D. W. Kirk and S. J. Thorpe, *International Journal of Hydrogen Energy*, 2007, *32(3)*, 359–364.

36 A. Motori and F. Sandrolini, *Journal of Power Sources*, 1994, *48(3)*, 361–370.

37 https://fityk.nieto.pl

38 L. Geerts, S. Cosentino, T.-W. Liao, A. Yadav, P.-C. Lin, V. S. Zharinov, K.-J. Hu, A. Longo, L. M.C. Pereira, D. Grandjean, J. Rongé, P. Lievens and J. A. Martens, *Catalysis Today*, 2019, *334*, 59–67.

39 M. B. Stevens, L. J. Enman, A. S. Batchellor, M. R. Cosby, A. E. Vise, C. D. M. Trang, and S. W. Boettcher, *Chemistry of Materials*, 2017, *29(1)*, 120–140

40 E. Arciga-Duran, Y. Meas, J.J. Perez-Bueno, J.C. Ballesteros and G. Trejo, *Electrochimica Acta*, 2018, *268*, 49–58.

41 V. C. Hoang, K. N. Dinh and V. G. Gomes, *Carbon*, 2020, *157*, 515–524.

42 O. D.-Morales, D. F.-Suspedra and M. T. M. Koper, *Chemical Science*, 2016, *7(4)*, 2639–2645.

43 Z. Xue, X. Zhang, J. Qin and R. Liu, *Journal of Materials Chemistry A*, 2019,*7(40)*, 23091–23097.

44 P. Oliva, J. Leonardi, J. F. Laurent, C. Delmas, J. J. Braconnier, M. Figlarz, and A. D. Guibert, *Journal of Power Sources*, 1982, *8*, 229–255.

45 D. G. Evans and R. C. Slade, *Layered double hydroxides*, Springer, 2006, 1–87.

46 B. Wang, C. Tang, H.-F. Wang, X. Chen, R. Cao and Q. Zhang, *Advanced Materials*, 2019, *31(4)*, 1805658.

47 T. Shinagawa, A. T. Garcia-Esparza and K. Takanabe, *Scientific Reports*, 2015, *5*, 13801.

48 S. Trasatti, *Electrochimica Acta*, 1991, *36(2)*, 225–241.

49 V. D. Silva , T. A. Simones, J. P. F. Grilo, E. S. Medeiros, and D. A. Macedo, *Journal of Materials Science*, 2020, *55(15)*, 6648–6659.

50 M. Gao, W. Sheng, Z. Zhuang, Q. Fang, S. Gu, J. Jiang, and Y. Yan, *Journal of the American Chemical Society*, 2014, *136(19)*, 7077–7084.

View Article Online
DOI: 10.1039/D0MA00467G

51 Y. Zhao, X. Jia, G. Chen, L. Shang, G. I.N. Waterhouse, L.-Z. Wu, C.-H Tung, D. O'Hare and T. Zhang, *Journal of the American Chemical Society*, 2016, *138(20)*, 6517–6524.

52 P.T. Babar, A.C. Lokhande, M.G. Gang, B.S. Pawar, S.M. Pawar and J. H. Kim, *Journal of Industrial and Engineering Chemistry*, 2018, *60*, 493–497.

53 A. C. Pebley, E. Decolvenaere, T. M. Pollock and M. J. Gordon, *Nanoscale*, 2017, 9(39), 15070–15082.

54 X. Zhou, Z. Xia, Z. Zhang, Y. Ma and Y. Qu, *Journal of Materials Chemistry A*, 2014, *2(30)*, 11799–11806.

55 F. E. S. Oztuna, T. Beyazay, and U. Unal, *Journal of Physical Chemistry C*, 2019, *123(46)*, 28131–28141.

56 L. Tong, W. Wu, K. Kuepper, A. Scheurer, and K. Meyer, *ChemSusChem*, 2018, *11(16)*, 2752–2757.

57 N. Cheng, Q. Liu, J. Tian, X. Sun, Y. He, S. Zhai, A. M. Asiri*, International Journal of Hydrogen Energy*, 2015, *40(32)*, 9866–9871.

58 W. Yuan, C. Li, M. Zhao, J. Zhang, C. M. Li and S. P. Jiang, Electrochimica Acta, 2020, 342, 136118

59 A. Scandurra, A. Porto, L. Mameli, O. Viscuso, V. Del Bo and S. Pignataro, *Surface and Interface Analysis*, 1994, 22*(1-12)*, 353–357.

60 M. C. Biesinger, B. P. Payne, L. W. M. Lau, A. Gerson and R. St. C. Smart, Surface and Interface Analysis, 2009, *41(4)*, 324–332.

61 A. P. Grosvenor, M. C. Biesinger, R. St. C. Smart and N. S. McIntyre, *Surface Science*, 2006, *600(9)*, 1771–1779.

View Article Online
DOI: 10.1039/D0MA00467G

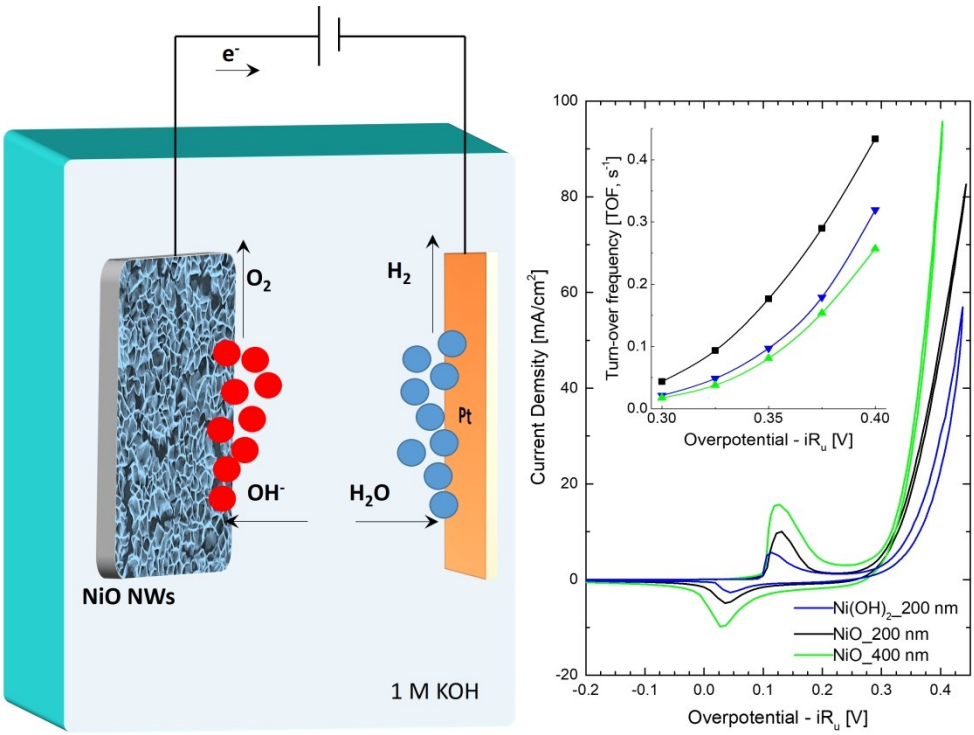

254x190mm (300 x 300 DPI)

View Article Online
DOI: 10.1039/D0MA00467G

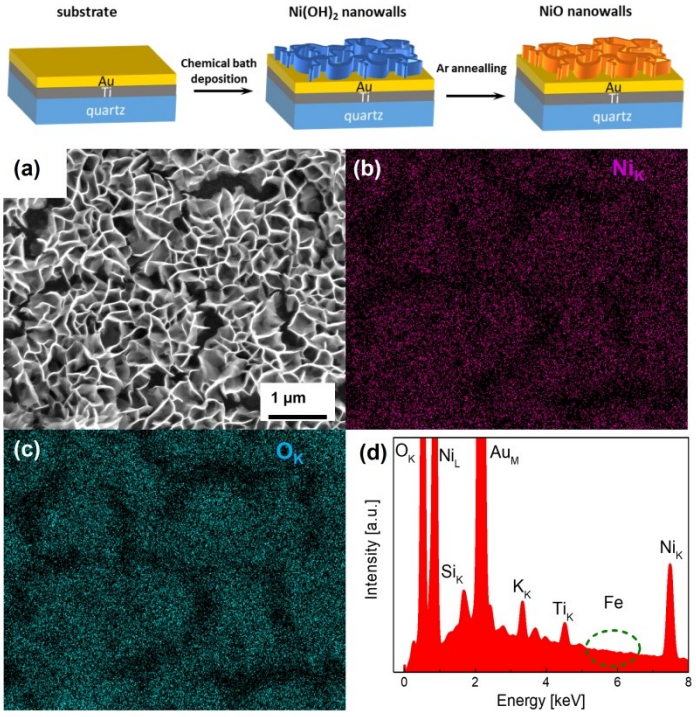

Figure 1: SEM image of NiO NW (a), and corresponding EDX-SEM color map for Ni (b) and O (c) atomic signals, together with EDX survey (d).

254x190mm (300 x 300 DPI)

View Article Online
DOI: 10.1039/D0MA00467G

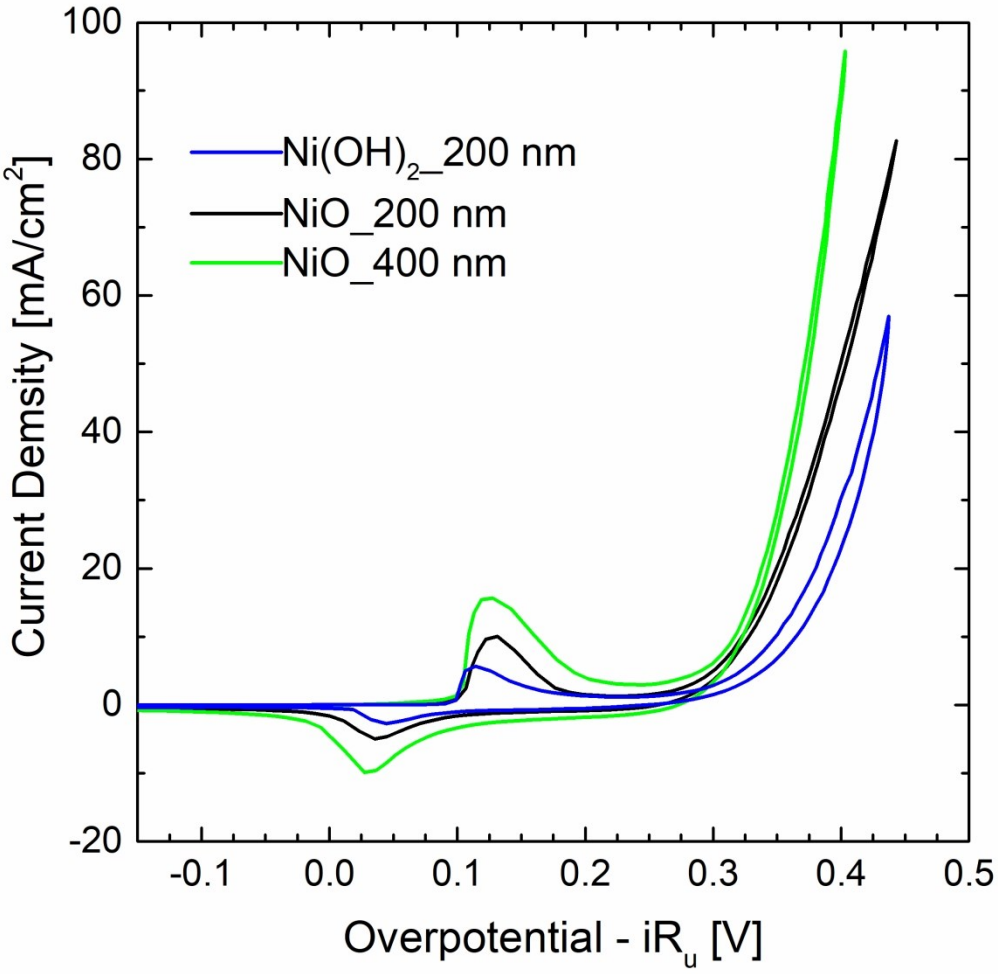

Figure 2: Cyclic voltammetry curves of Ni(OH)2 and NiO NW films deposited on Au/Ti/quartz substrates. All curves refer to the 10th cycle and overpotential was corrected for the uncompensated resistance estimated from EIS measurements.

209x208mm (300 x 300 DPI)

View Article Online
DOI: 10.1039/D0MA00467G

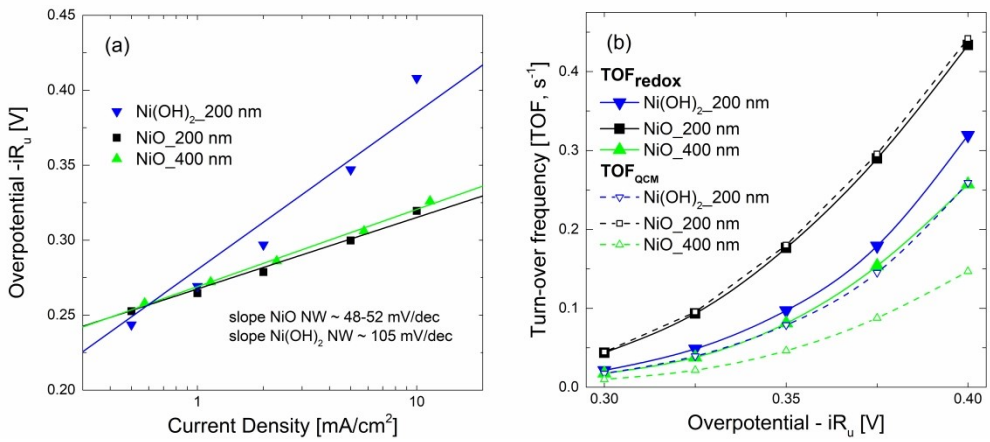

Figure 3: Steady-state Tafel plots (a) and turn-over frequency (TOF) curves (b) of Ni(OH)2 and NiO NWs films. The values of overpotential of Tafel analysis were acquired from CP measurements in steps from 0.05 mA/cm2 to 10 mA/cm2, each held for 3 min. TOFredox values were calculated considering the number of active sites extracted from electrochemical measurements, or measured by QCM (TOFQCM).

635x279mm (300 x 300 DPI)

View Article Online
DOI: 10.1039/D0MA00467G

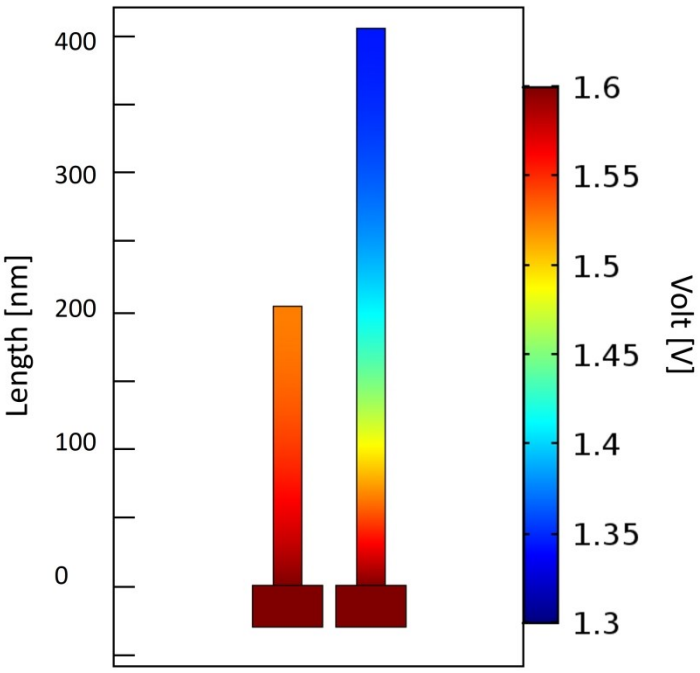

Figure 4: Electric potential distribution in the NiO NW electrodes with different NW size in 1 M KOH solution for 1.6 V of applied bias, as simulated by COMSOL Multiphysics software. A 20 nm thick and 200 (or) 400 nm tall NiO nanosheet was used to simulate the NiO nanowalls electrodes.

254x190mm (300 x 300 DPI)

View Article Online
DOI: 10.1039/D0MA00467G

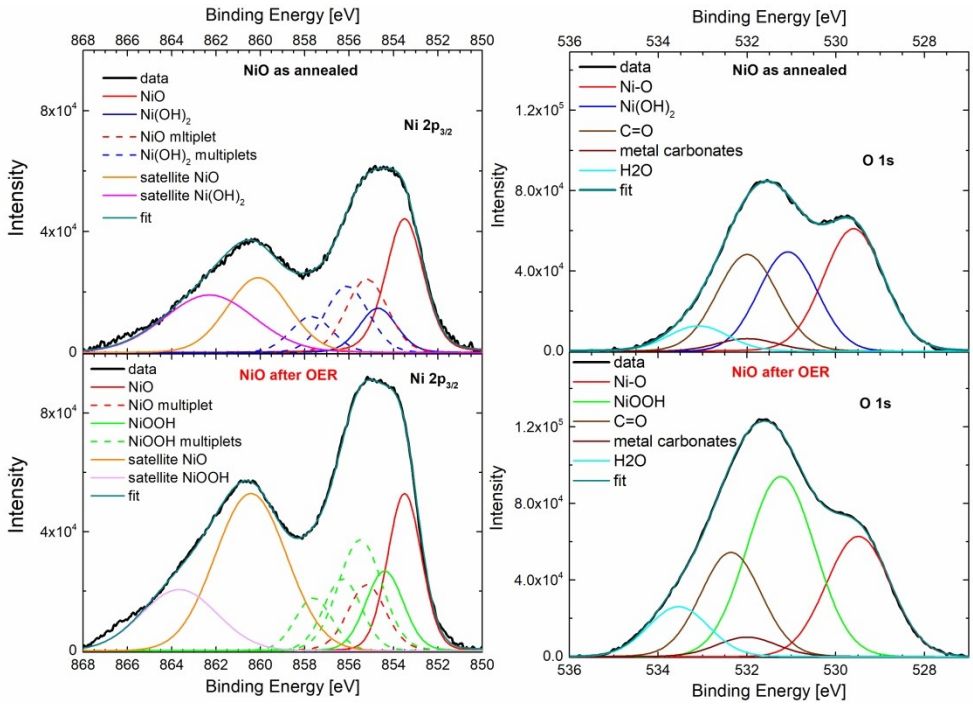

289x202mm (300 x 300 DPI)